Simulating the Ion Precipitation from the Inner Magnetosphere by H-band and He-band Electro Magnetic Ion Cyclotron (EMIC) Waves

Shreedevi P R[1], Yiqun Yu[2], Binbin Ni[3], Anthony Saikin[4], and Vania K Jordanova[5]

[1]School of Space and Environment, Beihang University, Beijing
[2]Beihang University
[3]Department of Space Physics, School of Electronic Information, Wuhan University
[4]University of California
[5]Space Science and Application, Los Alamos National Laboratory

November 21, 2022

Abstract

During geomagnetic storms, magnetospheric wave activity drives the ion precipitation which can become an important source of energy flux into the ionosphere and strongly affect the dynamics of the Magnetosphere-Ionosphere (MI) coupling. In this study, we investigate the role of Electro Magnetic Ion Cyclotron (EMIC) waves in causing ion precipitation into the ionosphere using simulations from the RAM-SCBE model with and without EMIC waves included. The global distribution of H-band and He-band EMIC wave intensity in the model is based on three different EMIC wave models statistically derived from satellite measurements. Comparisons among the simulations and with observations suggest that the EMIC wave model based on recent Van Allen Probes observations is the best in reproducing the realistic ion precipitation into the ionosphere. Specifically, the maximum precipitating proton fluxes appear at L=4-5 in the afternoon-to-night sector which is in good agreement with statistical results, and the temporal evolution of integrated proton energy fluxes at auroral latitudes is consistent with earlier studies of the stormtime precipitating proton energy fluxes and vary in close relation to the Dst index. Besides, the simulations with this wave model can account for the enhanced precipitation of <20 keV proton energy fluxes at regions closer to earth (L<5) as measured by NOAA/POES satellites, and reproduce reasonably well the intensity of <30 keV proton energy fluxes measured by DMSP satellites. It is suggested that the inclusion of H-band EMIC waves improves the intensity of precipitation in the model leading to better agreement with the NOAA/POES data.

Simulating the Ion Precipitation from the Inner Magnetosphere by H-band and He-band Electro Magnetic Ion Cyclotron (EMIC) Waves

P. R. Shreedevi[1], Yiqun Yu[1,2], Binbin Ni[3], Anthony Saikin[4], Vania K. Jordanova [5]

[1]School of Space and Environment, Beihang University, Beijing
[2]Key Laboratory of Space Environment Monitoring and Information Processing, Ministry of Industry and Information Technology, Beijing, China
[3]Department of Space Physics, School of Electronic Information, Wuhan University, China
[4]University of California, Los Angeles, CA, USA
[5]Space Science and Application, Los Alamos National Laboratory, Los Alamos, NM, United States

Key Points:

- Three different empirical EMIC wave models are used in the simulation.
- A recent Van Allen Probes data-based EMIC wave model produces precipitation patterns consistent with statistical and in-situ observations.
- The inclusion of H-band EMIC waves enhances precipitation intensity, leading to better agreement with data.

Corresponding author: Yiqun Yu, yiqunyu17@gmail.com

Abstract

During geomagnetic storms, magnetospheric wave activity drives the ion precipitation which can become an important source of energy flux into the ionosphere and strongly affect the dynamics of the Magnetosphere-Ionosphere (MI) coupling. In this study, we investigate the role of Electro Magnetic Ion Cyclotron (EMIC) waves in causing ion precipitation into the ionosphere using simulations from the RAM-SCBE model with and without EMIC waves included. The global distribution of H-band and He-band EMIC wave intensity in the model is based on three different EMIC wave models statistically derived from satellite measurements. Comparisons among the simulations and with observations suggest that the EMIC wave model based on recent Van Allen Probes observations is the best in reproducing the realistic ion precipitation into the ionosphere. Specifically, the maximum precipitating proton fluxes appear at L=4-5 in the afternoon-to-night sector which is in good agreement with statistical results, and the temporal evolution of integrated proton energy fluxes at auroral latitudes is consistent with earlier studies of the stormtime precipitating proton energy fluxes and vary in close relation to the Dst index. Besides, the simulations with this wave model can account for the enhanced precipitation of <20 keV proton energy fluxes at regions closer to earth (L<5) as measured by NOAA/POES satellites, and reproduce reasonably well the intensity of <30 keV proton energy fluxes measured by DMSP satellites. It is suggested that the inclusion of H-band EMIC waves improves the intensity of precipitation in the model leading to better agreement with the NOAA/POES data.

1 Introduction

Particle precipitation into the Earth's atmosphere is known to affect the ionospheric conductances [*Hardy et al.*, 1989; *Galand et al.*, 2001; *Lyons*, 1992; *Cowley*, 2000; *Ridley et al.*, 2004; *Merkin et al.*, 2005; *Yu et al.*, 2016, 2018; *Chen et al.*, 2019, and references therein] and play a major role in modulating the ionospheric dynamics especially during geomagnetically disturbed periods [*Prölss*, 1995; *Shreedevi et al.*, 2016]. Gaining insight into the mechanisms that modulate the precipitating fluxes and by that means the energy input into the ionosphere is hence of utmost importance for advancing our understanding of the Magnetosphere-Ionosphere (MI) coupling physics. Although the electron precipitation is considered to be a major source of energy flux into the ionosphere, the contribution of ions to the total energy flux is on average about 15 percent of that of electrons [*Hardy et al.*, 1989] and cannot be neglected [*Lui et al.*, 1977; *Galand et al.*, 2001; *Frey*, 2007;

Tian et al., 2020]. Numerous studies have documented the presence of a permanent region of precipitating isotropic ion fluxes (known as the proton aurora oval) roughly colocated with the region of electron produced auroral oval at higher auroral latitudes [*Sergeev et al.*, 1983; *Sergeev and Newell*, 1997]. A second region of localized precipitation of energetic protons (LPEP) (anisotropic fluxes) has also been observed at latitudes equatorward of the boundary of the isotropic fluxes [*Hultqvist et al.*, 1976; *Yahnin and Demekhov*, 2018; *Semenova et al.*, 2019]. The role of precipitating ion fluxes becomes especially important within the regions of anisotropic ion fluxes where the precipitating energy carried by ions can become comparable to that of electrons [*Hardy et al.*, 1989; *Lui et al.*, 1977; *Jordanova et al.*, 1996; *Galand et al.*, 2001; *Frey*, 2007; *Jordanova*, 2011; *Tian et al.*, 2020].

While most of our knowledge regarding the proton precipitation pattern and its relation to the external driving mechanisms and the magnetic activity are based on the studies of the precipitating ion fluxes in the proton auroral oval [*Hardy et al.*, 1989; *Newell et al.*, 2009; *Vorobjev and Antonova*, 2015], significant efforts are being laid to understand the spatial distribution and occurrence pattern of the LPEP [*Semenova et al.*, 2019, and references therein]. There has been increasing evidence in the form of several statistical/case studies as well as numerical modeling studies that relate the precipitation of ion fluxes at regions equatorward of the isotropic boundary to the presence of EMIC waves in the magnetosphere [*Cornwall et al.*, 1970; *Soraas et al.*, 1980, 1999; *Jordanova et al.*, 1997, 2001; *Morley et al.*, 2009; *Ni et al.*, 2016; *Popova and Chernyaeva*, 2018; *Semenova et al.*, 2019]. The appearance of the detached subauroral proton arcs, cusp proton aurora events, subauroral proton auroral flashes and subauroral proton spots are related to the precipitation loss of protons into the ionosphere caused by the pitch angle scattering of ring current ions by EMIC waves [*Jordanova et al.*, 2007; *Sakaguchi et al.*, 2008; *Ni et al.*, 2016]. EMIC waves are known to occur during magnetic disturbances, from the temperature anisotropy of the freshly injected medium energy ring current ions (1-100keV) into the inner magnetosphere [*Jordanova et al.*, 2001] or by rapid compression of the dayside magnetosphere owing to solar wind dynamic pressure fluctuations [*Usanova et al.*, 2012]. EMIC waves propagate at frequencies below the proton gyrofrequency and are usually classified into the Hydrogen (frequencies between He+ gyrofrequency and the H+ gyrofrequency), Helium (frequencies between He+ gyrofrequency and O+ gyrofrequency) and Oxygen (frequencies below O+ gyrofrequency) bands based on the ion gyrofrequency.

Statistical studies using satellite measurements have explored in detail the occurrence rates and spatial distribution of the EMIC waves in the magnetosphere for different space weather conditions. These studies suggest predominant EMIC wave occurrences in the prenoon (08<MLT<11) and the dusk sector (13<MLT<18), with the occurrence rates increasing for higher L values [*Korth et al.*, 1984; *Usanova et al.*, 2012; *Saikin et al.*, 2015]. The peak in the occurrence rates appearing at large equatorial distances (L>7) in the prenoon sector is often associated with the dayside magnetospheric compressions [*Usanova et al.*, 2012] while the peak in the dusk sector is related to the ion anisotropy driven by the onset of magnetic disturbances [*Saikin et al.*, 2016]. Although EMIC wave events are known to occur increasingly during the onset and the main phase of geomagnetic storms [*Halford et al.*, 2016; *Keika et al.*, 2013; *Meredith et al.*, 2014; *Saikin et al.*, 2016; *Usanova et al.*, 2012], observations have shown the presence of non-storm/quiet time EMIC waves as well. The quiet time EMIC waves are often observed in the dawn to afternoon sector with peak occurrences around 11-12 MLT [*Park et al.*, 2016; *Saikin et al.*, 2016]. Hydrogen band waves are reported to occur frequently (about 10%) in the afternoon sector at higher L values (7<L<9) irrespective of the magnetic activity, while Helium band waves show higher occurrence rates (5-10%) in the prenoon to dusk sector in the inner magnetosphere (4<L<7) especially during periods of high magnetic activity [*Keika et al.*, 2013].

Theoretical/simulations studies conducted in the past have provided a broad understanding of the role of EMIC waves in modulating the particle dynamics in the inner magnetosphere and precipitating fluxes in the ionosphere [*Cornwall et al.*, 1970; *Horne and Thorne*, 1994; *Jordanova et al.*, 2001, 2007; *Meredith et al.*, 2014; *Usanova et al.*, 2012; *Horne and Thorne*, 1993]. Theoretical calculations have shown that EMIC wave convective growth rate enhances in the regions with high background cold plasma density as it leads to lower parallel resonant energy between the instability and hot anisotropic ions [*Cornwall et al.*, 1970]. The favoured regions for the EMIC wave generation are thus the regions in the vicinity of the plasmapause and the plasmaspheric drainage plume [*Cornwall et al.*, 1970; *Jordanova et al.*, 2001; *Saikin et al.*, 2018]. EMIC waves are shown to be easily excited in the regions of low magnetic field (magnetic equator <11 MLAT) from where they could propagate into the high latitudes along the magnetic field lines [*Horne and Thorne*, 1993, 1994; *Loto'aniu et al.*, 2005]. They are observed as ultralow frequency Pc1-Pc2 (0.1-5Hz) pulsations from the ground with high wave occurrence rates even during the late recovery phase of geomagnetic storms [*Yahnina et al.*, 2003].

The storm time morphology of EMIC wave-induced proton precipitation has been studied by *Jordanova et al.* [2001, 2006] using the RAM-SCB model. They demonstrated that the gyroresonant interaction of the EMIC waves results in the pitch angle scattering of the ring current ions into the loss cone and causes significant proton precipitation in the postnoon sector during geomagnetic storms. They calculated the convective EMIC wave growth self-consistently with the evolving ring current ion populations and applied an empirically based relation to derive the corresponding EMIC wave amplitudes required to calculate the pitch angle diffusion coefficients.They however analysed only the effects of He-band EMIC waves on the proton precipitation. In a similar study *Khazanov et al.* [2007] used the RC/EMIC model to understand the ring current ion losses induced by EMIC waves. Both these studies suggested that an accurate representation of the proton precipitation morphologies in the models require a better representation of the wave parameters as the interaction of the EMIC waves and the ring current ions are sensitive to the wave parameters. Recent studies using various satellite measurements have provided different statistical models of the spectral properties of the H-band and He-band EMIC waves that can be used as input for modeling the MI coupling physics. In this paper, we extend the initial study by *Jordanova et al.* [2001] by including for the first time the effects of H-band EMIC waves on proton precipitation. We simulate the geomagnetic storm of 31 August 2005 using the RAM-SCBE model with three different EMIC wave models based on :(1) time averaged intensity of EMIC waves from Combined Release and Radiation Effects (CRRES) satellite measurements, (2) realistic EMIC wave frequency spectra constructed using measurements from the Van Allen Probes, and (3) EMIC wave intensities obtained from the Van Allen Probes measurements. To assess the ability of the three EMIC wave models in producing realistic precipitation into the ionosphere, the results are compared with particle measurements from NOAA/POES and DMSP satellites.

2 RAM-SCBE Model Description

The RAM-SCBE model, i.e., the ring current atmosphere interactions model (RAM) coupled with a self-consistent (SC) magnetic field (B) and electric field (E) code [*Jordanova et al.*, 2006, 2010; *Zaharia et al.*, 2006; *Yu et al.*, 2017] used in this study, computes the kinetic physics of charged particles in the inner magnetosphere by solving the bounce-averaged Fokker-Planck equation for the phase space distribution function $F_l(t, R_o, \phi, E, \alpha)$ of a given ring current species l given by:

$$\frac{\partial F_l(t,R_o,\phi,E,\alpha)}{\partial t} + \frac{1}{R^2}\frac{\partial}{\partial R_o}(R_o^2\langle\frac{dR_o}{dt}\rangle F_l) + \frac{\partial}{\partial \phi}(\langle\frac{d\phi}{dt}\rangle F_l)$$
$$+\frac{1}{\gamma p}\frac{\partial}{\partial E}(\gamma p\langle\frac{dE}{dt}\rangle F_l) + \frac{1}{h\mu_o}\frac{\partial}{\partial \mu_o}(h\mu_o\langle\frac{d\mu_o}{dt}\rangle F_l) \tag{1}$$
$$= \langle(\frac{\partial F_l}{\partial t})_{loss}\rangle$$

where

R_o is the radial distance in the magnetic equatorial plane,

E is the kinetic energy of the particle which varies from 0.15 keV to 400 keV,

μ_o is the cosine of the equatorial pitch angle α_o, α varies from 0 to 90° ,

ϕ is the geomagnetic east longitude,

p is the relativistic momentum of the particle,

γ is the Lorentz factor,

h(μ_o) is proportional to the bounce path length in the magnetic field.

The RAM code computes the distribution functions for the three major ring current species (e.g., H+, He+ and O+) and electrons at all pitch angles and magnetic local times within the radial distance of 2-6.5 R_E in the magnetic equatorial plane. The time-dependent plasma boundary conditions, magnetic field and electric field are required for the time-evolution of the phase space distribution function. In the RAM model, the plasma boundary conditions at 6.5 R_e are specified using the in-situ measurements of energetic flux from the LANL geosynchronus satellites. The measured ion fluxes are divided between the three major ring current ion species using the formulation by *Young et al.* [1982] and vary as a function of the K_p index. The magnetic field in the RAM code is obtained from its self-consistent coupling with a 3-D Euler-potential based equilibrium code which uses the plasma pressure produced by the ring current particles to estimate the magnetic field [*Zaharia et al.*, 2006]. The electric field needed in the ring current model is derived by mapping the electric potential in the mid-latitude ionosphere onto the equatorial plane in the inner magnetosphere [*Yu et al.*, 2017]. The electric potential is solved from ionospheric conductance, determined based on electron precipitation due to wave-particle interactions, and field-aligned currents, determined from the pressure gradient using the Vasyliunas formula [*Vasyliunas*, 1970]. In this way the ring current model is driven by a self consistent electric field along with a self-consistent magnetic field. Under the influence of the electric field and magnetic field, the plasma at the nightside boundary drifts towards the earth where it undergoes various acceleration and loss processes.

The dominant loss processes for both ring current ions and electrons are included in the model [*Jordanova et al.*, 2012]. The loss of electrons from the inner magnetosphere occurs mainly through precipitation into the upper atmosphere and wave-particle interactions. The pitch angle scattering of electrons by whistler mode chorus and hiss waves are incorporated in the model. The important loss processes for ions in the ring current model include charge exchange with neutral hydrogen geocorona, precipitation loss due to widening of the loss cone and scattering by EMIC waves. The scattering of ring current ions by EMIC waves is treated as a diffusive process in the RAM-SCBE model:

$$\langle(\frac{\partial F_l}{\partial t})\rangle = \frac{1}{h\mu_o}\frac{\partial}{\partial \mu_o}\left[h\mu_o\langle D_{\mu_o\mu_o}\rangle\frac{\partial F_l}{\partial \mu_o}\right] \tag{2}$$

$$\langle D_{\mu_o\mu_o}\rangle = (1-\mu_o^2)\langle D_{\alpha\alpha}\rangle \tag{3}$$

where $\langle D_{\alpha\alpha}(E,\alpha)\rangle$ is the bounce averaged pitch angle diffusion coefficient associated with wave particle interaction obtained via the quasi linear theory.

In the present study, the EMIC wave amplitudes needed to calculate the quasi-linear diffusion coefficients are obtained from EMIC wave models statistically derived from satellite measurements. We conduct simulations of the ion precipitation with three different EMIC wave models. The wave model 1 is based on the time averaged intensity of EMIC waves from Combined Release and Radiation Effects (CRRES) satellite measurements [*Kersten et al.*, 2014]. The wave model 1 provides the H-band and He-band EMIC wave intensities in the 1200-1800 MLT sector only. For varying levels of geomagnetic activity as indicated by the Kp index, the distribution of EMIC wave intensities in the wave model 1 is as shown in Figure 1. In this model, both the H-band and He-band EMIC wave activity increases as the geomagnetic activity strengthens. The He-band waves, however, are predominant in the inner magnetosphere during all levels of geomagnetic activity with high intensities around ~L=5. Note that the CRRES satellite measurements used in the wave model 1 are from a period of 15 months during 25 July 1990 to 11 October 1991.

The wave model 2 is derived from the statistical EMIC wave frequency spectra constructed using the Van Allen Probes measurements from September 2012 to December 2015

[*Zhang et al.*, 2016]. The EMIC wave spectra within each band in the wave model 2 is expressed as:

$$y = \sum_{i=0}^{2} a_{i0} exp\left(- \frac{(f - a_{i1})^2)}{a_{i2}} \right) exp\left(- \frac{(m - a_{i3})^2)}{a_{i4}} \right) \quad (4)$$

where,

y is the magnetic wave intensity (nT^2/Hz),

f is the normalized wave frequency ($\frac{f_w}{f_{cp}}$),

m is the normalized MLT ($\frac{MLT}{24}$)

a_{i0},a_{i1},a_{i2},a_{i3} and a_{i4} are the fitting parameters and provided in *Zhang et al.* [2016].

The statistical wave frequency spectra is parameterized by $\frac{f_{pe}}{f_{ce}}$ and MLT and does not show any dependence on L shell. After integrating over the associated frequency band, the H-band and He-band EMIC wave intensities for different ranges of $\frac{f_{pe}}{f_{ce}}$ are obtained and are as shown in panel (a) and (b) of Figure 2 respectively. In this model, the He-band EMIC waves predominates regions of high $\frac{f_{pe}}{f_{ce}}$ whereas the H-band EMIC waves are most active in the regions of low $\frac{f_{pe}}{f_{ce}}$.

The wave model 3 is based on the statistical distribution of EMIC wave intensities from the Van Allen Probes measurements during the period August 2014-June 2016 [*Saikin*, 2018]. The H-band and He-band EMIC wave intensities in the wave model 3 are parameterized by the AE index and distributed in L-MLT as shown in Figure 3. The wave model 3 along with the distribution of EMIC waves from magnetically disturbed periods includes the quiet time EMIC waves that are known to appear due to the changes in the solar wind pressure. The wave activity in the model shows clear L-MLT dependence. For low levels of magnetic disturbance, the H-band waves in the model appear to be more active with higher intensities in the prenoon period. As the level of disturbance increases, there is an overall increase in the He-band wave intensity especially at regions closer to the earth. The EMIC wave activity in the model is strongest during highly disturbed periods (high AE index) at ∼L=4 in the afternoon-to-dusk sector.

3 Results

To examine the effects of scattering by EMIC waves on the ion precipitation, we simulated the 31 August 2005 geomagnetic storm using the RAM-SCBE model with and without

EMIC waves included. The solar wind and geomagnetic conditions during 31 May 2005 are shown in panels (a)-(e) of Figure 4. The geomagnetic storm of 31 August 2005 was initiated by the arrival of a CME driven shock at the magnetosphere. In response to the interplanetary shock, the solar wind dynamic pressure is seen to enhance steadily and reach its peak value at ∼1400UT. The southward turning of IMF Bz at ∼1200 UT led to the associated decrease in the Dst index which marks the onset of the geomagnetic storm. The main phase of the intense storm lasted for ∼8 hours with the Dst index reaching a minimum of -115nT at∼1900UT. The AE and AL indices are observed to exhibit rapid enhancements during the main phase of the storm. During the recovery phase that followed, the solar wind pressure, and the AE/AL indices are seen to return gradually to their quiet time values.

Figure 5(a) shows the pitch angle diffusion coefficients due to H-band and He-band EMIC waves at L=5 with f_{pe}/f_{ce}=14. These coefficients based on a nominal wave amplitude of 1.0 nT are scaled in the RAM-SCBE model depending on the local wave amplitude as well as the local value of f_{pe}/f_{ce} at a given location. It is seen that the diffusion coefficients due to H-band EMIC waves are highest at lower energies (<10 keV) while that due to He-band EMIC waves are highest at intermediate energies (10-100 keV) given at a certain pitch angle. Such a distribution indicates that the scattering efficiency of H-band EMIC waves is large for protons with lower energies while that of He-band EMIC waves is large for protons with energies of few tens to a few hundreds of keV. In the RAM-SCBE simulations, the diffusion coefficients depend on several factors like the wave intensity of H-band and He-band EMIC waves, the background plasma conditions and the magnetic field strength. The global distribution of diffusion coefficients due to H-band and He-band EMIC waves in the RAM-SCBE simulations with the EMIC wave models 1, 2 and 3 are shown in Figure 5(b). The plots are chosen at 1400 UT ie., during the main phase of the storm on 31 August 2005 and for protons with energy of ∼50 keV and pitch angle of ∼53°. In general, the pitch angle diffusion induced by He-band EMIC waves is stronger than that caused by H-band EMIC waves except for regions in the midnight sector where the He-band EMIC wave intensities are weak (wave model 2 and 3) or absent (wave model 1). The regions of maximum pitch angle diffusion in Figure 5(b) corresponds to regions of intense EMIC wave activity in the respective wave models which is (1) at L=3-5 in the 1200<MLT<1800 sector in wave model 1, and (2) at L=3-5 in the noon-to-midnight sector in wave model 2 and 3. Note that among the three wave models the pitch angle diffusion due to both H-band and He-band EMIC waves is the strongest in the simulations with the wave model 3.

The global distribution of the precipitating proton flux at three energies (E= ∼5 keV, ∼50keV and ∼164keV) obtained from the RAM-SCBE simulations with and without EMIC waves is shown in Figure 6. The plots are chosen at 1400 UT on 31 August 2005. The black dots in the plots represent the plasmapause boundary. In agreement with the previous studies [e.g. *Jordanova et al.*, 2001], in the absence of EMIC wave scattering, the precipitating proton fluxes are observed mostly in the midnight sector with maximum fluxes at L=5-6 as seen in panel (i). The proton fluxes obtained from the simulations with the EMIC wave models 1, 2 and 3 are shown in panels (ii)-(iv) of Figure 6 respectively. There are considerable changes in the spatial location and magnitude of the precipitating proton fluxes as compared to that obtained without EMIC waves. Additional regions of precipitation appear in the vicinity of the plasmapause (1) in the 1200<MLT<1800 sector in the simulation with wave model 1, and (2) in the noon-midnight sector for simulations with wave model 2 and 3, as a result of the enhanced pitch angle diffusion of protons (see Figure 5(b)) induced by the EMIC wave scattering. In the simulation with wave model 1, the proton precipitation increases significantly at ∼L=4-6 in the 1200-1800 MLT sector. The medium energy protons seem to be the most affected by the wave-particle interactions and dominate the precipitation with maximum fluxes at L=4-5. The new precipitating proton fluxes are about an order of magnitude higher than that obtained in the case without EMIC waves demonstrating that the wave particle interactions can cause enhancements in the proton precipitation.

The precipitation morphology simulated using the wave models 2 and 3 shows that the EMIC wave induced precipitation of low energy protons largely occurs in the vicinity of the plasmapause at regions between L=3-6 in the nightside. The largest fluxes of medium energy protons are observed closer to the earth (L=4-5) in the afternoon-to-midnight sector, within regions where the energetic ring current overlaps with the plasmaspheric population and the EMIC wave intensities are maximum in the respective wave models. The diffusion coefficients shown in Figure 5 suggests that the H-band waves strongly interact with the E=5 keV protons in the nightside while the He-band wave efficiently scatter the protons of medium energy in the noon-midnight sector leading to their precipitation loss into the ionosphere. Significant enhancements are also observed in the high energy proton fluxes in the morning sector as well owing to the effects of pitch angle diffusion [*Jordanova et al.*, 1998]. As expected, the most intense fluxes appear in the RAM-SCBE simulations with wave model 3, indicating that the strength of the precipitation depends on the intensity of the

EMIC waves which in turn depends on the assumed EMIC wave model. The medium energy precipitating fluxes seem to be the most affected, with more than an order of increase in magnitude. Apart from that, the precipitation is also extended in the noon-midnight sector in the simulations with wave model 3, unlike (i) the case without EMIC waves, where the proton fluxes are weak and mostly confined to L>5, or (ii) the case with wave model 1, where the precipitation appears only in the 1200-1800 MLT sector.

In a recent study using the NOAA/POES observations, *Semenova et al.* [2019] showed that during periods of intense magnetic activity the precipitating proton fluxes enhance in the afternoon-to-midnight sector at regions closer to the earth. For the sake of direct comparison, in Figure 7 is shown the statistical intensity of the precipitating proton fluxes from NOAA/POES observations by *Semenova et al.* [2019]. We present here only the intensity of precipitating proton flux for AE > 300 nT as it corresponds to the magnitude of AE index at 1400 UT on 31 August 2005 (see panel (c) of Figure 4). The precipitating proton fluxes in Figure 7 are extended in the noon-midnight direction with maximum intensity at L=4-5. It is evident that the RAM-SCBE simulations using both wave model 2 and 3 reproduces reasonably well the stormtime proton precipitation while the distribution of precipitating proton fluxes obtained from simulations without EMIC waves does not capture the NOAA/POES observations at all. These comparisons show that the EMIC wave scattering can account for the enhanced precipitation at regions closer to the earth (L<5).

4 Energy Flux into the ionosphere

The energy input into the ionosphere due to ion precipitation caused by EMIC wave scattering is examined using the integrated precipitating energy flux obtained from the simulations with and without EMIC waves. Figure 8 (a)-(d) shows the precipitating proton energy flux at ionospheric altitudes during the main phase (1400 UT) of the 31 Aug 2005 storm simulated using the RAM-SCBE model without EMIC waves and with wave model 1, 2 and 3 respectively. The plasmapause location is represented by the black dots. In the absence of EMIC waves, the precipitating proton energy flux is concentrated in the midnight sector with peak value of $\sim$0.1 ergs cm^{-2} s^{-1}. The proton energy fluxes are known to sharply enhance in the evening-to-midnight sector during the main phase of a geomagnetic storm [*Hardy et al.*, 1989; *Soraas et al.*, 1999; *Yahnina and Yahnin*, 2014]. In a study of the stormtime proton precipitation, *Fang et al.* [2007] reported the presence of enhanced integrated proton energy fluxes with peak value of $\sim$6.6 ergs cm^{-2} s^{-1} in the evening sector during the main phase of the storm. Using global maps of integrated proton energy fluxes, they showed that the regions of maximum precipitation moves westward towards the dusk sector and equatorward as the Dst falls to its minimum value [*Fang et al.*, 2007]. The magnitude or the location of integrated proton energy fluxes produced in the absence of EMIC waves are not consistent with these observations.

The inclusion of EMIC waves in the RAM-SCBE model gives rise to significant changes in the integrated precipitating proton energy fluxes as shown in Figure 8 (b)-(d). Large enhancements in the proton energy fluxes are seen to appear in the regions of strong EMIC wave activity in the wave models 1, 2 and 3 respectively. Clearly, the simulations with wave model 3 produce the intense proton energy fluxes (>1 ergs cm^{-2} s^{-1}) extended westwards in the midnight-to-afternoon sector similar to that reported by *Fang et al.* [2007]. The simulated proton energy fluxes obtained with wave model 2 show a similar spatial distribution. However the peak fluxes are concentrated in the midnight sector whereas in the afternoon-to-dusk sector, the proton energy fluxes of lesser magnitude are prevalent. As for the simulations with wave model 1, the proton energy fluxes are concentrated in the 1200-1800 MLT sector, but of lesser magnitude (<1 ergs cm^{-2} s^{-1}) as compared to the other cases.

The temporal distribution of precipitating proton energy flux at 2100 MLT (pre midnight) and 0300 MLT (early morning) on 31 August 2005 obtained for the simulations with and without EMIC waves is shown in Figure 9. Among the four cases, the simulations without EMIC waves and with wave model 1 show similar distribution at 2100 MLT and 0300 MLT. This is because, alike the case without EMIC waves, in the wave model 1 also, the EMIC wave activity is absent at both 2100 MLT and 0300 MLT (see Figure 5). It is notable that the precipitation is weak and confined to higher latitudes in the absence of EMIC wave scattering. The inclusion of statistically averaged EMIC wave intensities from all MLT sectors (wave model 2 and 3) produces significant enhancements in the precipitation in both the premidnight and early morning periods during the stormtime. Since the ion sources drift in the westward direction into regions of strong EMIC wave activity, the precipitation is higher at 2100 MLT (pre-midnight period). There is comparatively lower precipitation in the early morning sector where the EMIC wave activity is low in the wave models 2 and 3.

The precipitation into the ionosphere is known to exhibit good correlation with the evolution of ring current and the plasma sheet dynamics during geomagnetic storms [*Yahnina and Yahnin*, 2014; *Fang et al.*, 2007]. The early main phase of the geomagnetic storm of 31 August 2005 (1200-1400 UT) was characterized by periods of strong southward IMF accompanied by high solar wind pressure. It can be seen from Figure 9 that the simulations with wave model 3 produce intense proton energy fluxes during the early main phase of the storm in both the pre-midnight and early morning sectors as expected under conditions of strong southward IMF/solar wind pressure [*Semenova et al.*, 2019]. The simulations with wave model 2 also shows similar features except in the early morning sector where precipitation is observed to enhance only after ∼1400UT. During the main phase of the storm, the EMIC wave induced precipitation in both sectors is seen to propagate to latitudes as low as 51°MLAT in line with the variation in the Dst index. The proton energy fluxes obtained from the simulations with wave model 3 are seen to weaken and gradually recede to higher latitudes after ∼1800 UT at 0300 MLT as expected during the periods of northward IMF [*Yahnina and Yahnin*, 2014; *Walt and Voss*, 2004]. This is not exactly the case in the simulations with wave model 2, where during the recovery phase of the storm, weak fluxes are seen to be distributed over a wider range of latitudes in the early morning sector.

5 Comparison with the satellite observations

In order to assess the ability of the three different EMIC wave models in reproducing the realistic particle precipitation into the atmosphere, we compare the simulation results with the NOAA/POES satellite observations in Figure 10. NOAA/POES satellites are sun synchronous low-altitude polar orbiting satellites and provide global measurements of the particle precipitation into the atmosphere. In this study, we use the total energy input determined from the proton fluxes in the energy range 1-20keV measured by the Total Energy Detector (TED) onboard NOAA/POES satellites. During the geomagnetic storm of 31 August 2005, four POES satellites were operational. In Figure 10(a) is shown the proton energy flux <20keV at different MLT sectors, mapped to the magnetic equator and arranged into bins of spatial resolution of 0.25Re and temporal resolution of 0.5h. NOAA/POES observations show large enhancements in the precipitation energy flux in the midnight (21<MLT<03) MLT sector with the onset of the storm on 31 August 2005. There is considerable enhancement of energy flux in the dusk and dawn MLT sectors, but at large distances (L>5.5). The precipitation is seen to increase in the dusk (15<MLT<21), midnight ($21<MLT<03$) and dawn ($03<MLT<09$) MLT sectors as the storm progresses to its main phase. As the Dst falls to its minimum value, the regions of precipitation are seen to move equatorward and reach closer to Earth at $\sim$L=3. In the noon ($9<MLT<15$) sector, precipitation is observed only after 1500 UT, mostly at regions greater than L=4.5 and is very weak in the recovery phase. During the recovery phase of the storm, precipitation weakens in all the MLT sectors and is mostly confined to regions greater than L=4.

Figure 10(b)-(d) shows the distribution of <20 keV proton energy fluxes obtained from the RAM-SCBE simulations with wave models 1, 2 and 3 respectively. The simulation with wave model 1 produces weak enhancements in the precipitation that appears only in the noon ($9<MLT<15$), dusk ($15<MLT<21$) and midnight ($21<MLT<03$) MLT sectors during the storm. Clearly, the spatial distribution or magnitude of these enhancements is not consistent with the observations by the NOAA/POES satellites. The simulation with wave model 2 produces intense precipitation in the dusk ($15<MLT<21$) and midnight ($21<MLT<03$) sector after $\sim$1400 UT, but only at higher L shells ($L>5$). In this case the precipitation is seen to move to lower L shells after $\sim$1500 UT and strengthen at L=4-5 during the late main to recovery phase of the storm. However, the simulation with wave model 2 neither reproduces the intensity or the spatial coverage of the precipitation in the dawn ($03<MLT<09$), noon ($9<MLT<15$) and dusk ($15<MLT<21$) MLT sectors as measured by the NOAA/POES satellites. In the simulation with wave model 3, intense precipitation appears at higher L shells ($L>5$), in the dusk ($15<MLT<21$) and midnight ($21<MLT<03$) MLT sectors with the onset of the storm. The regions of enhanced precipitation is seen to gradually move equatorward (L=3.75) after 1400 UT. The maximum precipitation appears at L=4-5 in the dusk ($15<MLT<21$) and midnight ($21<MLT<03$) sectors similar to the NOAA/POES observations, but after $\sim$1500 UT. Although of lower magnitude, simulations with wave model 3 also produce considerable enhancements in the dawn ($03<MLT<09$) and noon ($9<MLT<15$) MLT sector as opposed to wave model 1 and 2. The simulations with wave model 3 however fails to reproduce the precipitation at regions $L<4$ during the early main phase of the storm alike the other two models. From these comparisons, it is clear that the addition of statistically averaged EMIC wave intensities from all MLT sectors improves the precipitation in the model a lot but still slightly underestimates the magnitude and the spatial coverage. This could be because the simulated storm event (31 August 2005) occurred during a period of stronger EMIC wave activity than that represented by the statistical wave model 2 and 3. *Park et al.* [2013] using the CHAMP satellite data from the solar cycle 23

(2000-2010), showed that the occurrence of Pc1 pulsations was maximum during the years 2004-2005. Besides, the EMIC wave activity is known to be stronger during the declining phase of the solar cycle. The wave models 2 and 3 are however based on observations from the years 2012-2015 and 2014-2016 respectively, which include the solar maximum period of a relatively weaker solar cycle 24.

In order to delineate the role of the H-band/He-band EMIC waves in causing the precipitation of low energy protons, we conducted the RAM-SCBE simulation with only the He-band EMIC waves included from the wave model 3. The integrated precipitating energy flux of <20 keV protons from the simulation with He-band EMIC waves is shown in Figure 11(a). Clearly, the He-band waves alone cannot produce the intensity or the spatial coverage of the precipitation in any MLT sector as measured by the NOAA/POES satellites (shown in Figure 10(a)). To further analyze the contribution of the H-band EMIC waves, we calculated the difference of the <20 keV proton energy fluxes from the simulations with wave model 3 and the simulation with only the He-band waves included from the wave model 3. The difference in the energy flux shown in Figure 11(b) is notably higher in the 15-21, 21-03 and 03-09 MLT sectors during the main phase and the early recovery phase of the storm. This implies that the H-band waves strongly influence the precipitation of low energy protons (<20 keV) during the stormtime. The difference is maximum in the dusk-midnight sector at ∼L=4.5-5.5 further suggesting that the H-band EMIC waves dominate the precipitation of the <20 keV protons in the midnight sector during the 31 August 2005 storm. Finally, the intensity of precipitation induced by the H-band waves seem to agree with that measured by NOAA/POES satellites although the spatial coverage of the precipitation needs to improve in the model.

Measurements from the polar orbiting DMSP satellite are also examined as it follows a sun-synchronous dawn-dusk orbit at an altitude of 840 km, and therefore, is able to provide insight into the response of the topside mid latitude ionosphere. The SSJ/4 instrument onboard the DMSP satellites provides in situ measurements of the particle fluxes on 31 August 2005 in the energy range 30eV to 30keV in 1-s cadences. A comparison of the ion energy spectrograms and the integrated ion energy flux obtained from DMSP F16 satellite and the simulation results is provided in Figure 12(i)-(vi). The different subplots represent (i) the DMSP F16 ion energy spectrogram, (ii)-(v) ion energy spectrogram from simulation results and (vi) a comparison of the integrated ion energy flux from DMSP F16 and simulations with and without EMIC waves included. The plots are chosen at different MLTs in the dusk-midnight sector where intense ion precipitation is expected during magnetically disturbed periods.

The DMSP F16 ion energy spectrograms show significant enhancements in the energy fluxes especially in the dusk sector as expected during the main phase of a geomagnetic storm. As for the simulations without including EMIC waves, the energy flux is very weak (in the midnight sector) or absent (in the dusk sector). The simulation results with wave model 1 show similar results as the case without EMIC waves except in the dusk sector. This is because, EMIC wave activity and the associated pitch angle diffusion occur only in the 1200 to 1800 MLT sector in wave model 1. Furthermore, the simulations with wave model 2 is seen to produce significant precipitation in the dusk as well as midnight sector. However, the integrated ion energy fluxes simulated using wave model 2 are about an order of magnitude smaller than that observed by DMSP F16. Among the simulations with the three wave models, the magnitude of the precipitating proton energy fluxes and the integrated ion flux simulated using the wave model 3 agrees reasonably well with the DMSP measurements in the dusk as well as midnight sectors. However, the model does not capture the equatorward edge of the auroral oval, but instead produces a gradual decrease of the precipitating energy fluxes towards the lower latitudes. This is probably because of the under-shielding of electric field in the ring current model.

6 Summary and Conclusions

Understanding the causative mechanisms of particle precipitation and its role in modulating the energy flux deposited into the ionosphere is necessary to obtain accurate predictions of the storm time ionospheric dynamics. Although significant contributions to the total energy flux into the ionosphere can equally come from both electron and ion precipitation, the latter has received much less attention. In this paper, we examined the role of one causative mechanism of proton precipitation from the inner magnetosphere ie., EMIC wave scattering. We extended the initial study by *Jordanova et al.* [2001] by further including, for the first time, the effects from H-band EMIC waves on proton precipitation. We studied the ion precipitation into the ionosphere during the geomagnetic storm of 31 August 2005 using RAM-SCBE simulations with three different EMIC wave models that are based on (1) time averaged intensity of EMIC waves from Combined Release and Radiation Effects (CRRES) satellite measurements, (2) EMIC wave frequency spectra constructed using measurements from the Van Allen Probes, and (3) statistical distribution of EMIC wave intensities obtained from the Van Allen Probes. In order to assess the ability of the statistically derived EMIC wave models in producing the realistic particle precipitation into the atmosphere, the simulation results have been compared with the particle flux measurements from the DMSP and NOAA/POES satellites. The important results from this study are as follows:

1. The precipitating proton fluxes simulated with the wave model 3 show significant enhancements in the afternoon-to-midnight sector in the regions between L=4-5 during the main phase of the storm. These results are well in agreement with the statistical observations of global proton precipitation by *Semenova et al.* [2019].
2. In the presence of EMIC wave scattering, significant enhancements in the integrated proton energy fluxes appear at latitudes as low as 51° MLAT; the proton energy fluxes are weak and confined to higher latitudes in their absence. This suggests that the EMIC wave scattering of ring current ions gives rise to substantial enhancements in the proton energy flux at mid-latitude regions. The simulated proton energy fluxes are higher in the premidnight sector as compared to the early morning sector and vary in line with the strength of the Dst index. The magnitude and location of the integrated proton energy fluxes obtained from the simulations using wave model 3 are consistent with observations [e.g. *Fang et al.*, 2007] of the precipitating proton energy fluxes during stormtime.
3. A comparison of the <20keV proton energy flux obtained from the NOAA/POES satellite with the simulations shows that the EMIC wave, particularly the H-band that exerts diffusion on ions with a few to tens of keV can account for the enhanced proton precipitation especially at regions closer to the earth (L< 5). The RAM-SCBE simulations with wave model 3 improves the precipitation in all the MLT sectors but still slightly underestimates the magnitude and the spatial coverage. This discrepancy in the precipitation pattern could be because the simulated storm event i.e., 31 August 2005 occurred during a period of strong EMIC wave activity in the solar cycle 23 whereas the wave model 3 is based on the observations from a period of relatively weaker EMIC wave activity in the solar cycle 24.
4. The RAM-SCBE simulations with wave model 3 reproduce reasonably well the intensity of <30 keV proton energy fluxes at 840 km at several DMSP satellite passes in the dusk and midnight sectors. The model however does not capture the equatorward edge of the auroral oval, which may be attributed to the undershielding of the convective electric field in the model.

5. The wave model 3 emerged out to be the best in reproducing the realistic ion precipitation into the ionosphere as compared to the other two wave models. The wave model 2 also produces reasonably better precipitation patterns as compared to the wave model 1.

It should be noted that the EMIC wave-induced precipitating ion flux down to the ionosphere is not included in the calculation of ionospheric conductance in this study. A follow-on study will particularly examine its effect on the auroral conductance to strengthen the self-consistency in the model. In addition, recently *Yu et al.* [2020] investigated the effect of another ion scattering mechanism, i.e., the field line curvature (FLC) scattering, in precipitating ions down to the ionosphere. We will in the future explore the relative contribution of these two ion scattering mechanisms and contribution of associated ion precipitation to the ionospheric conductance, in order to obtain a more comprehensive insight of the MI coupling physics.

Acknowledgments

This work is supported by the National Natural Science Foundation of China grants 41974192, 41821003 and 4191101142. The authors thank NASA/GSFC CDAWeb team and the WDC-C2 (Kyoto) for the interplanetary data, auroral electrojet and geomagnetic indices data (http://cdaweb.gsfc.nasa.gov). The authors gratefully acknowledge the NOAA website for providing POES data and the DMSP data. These datsets can be accesses at http://satdat.ngdc.noaa.gov/sem/poes/ and http://www.ngdc.noaa.gov/stp/satellite/dmsp/. Work at Los Alamos was conducted under the auspices of the U.S. Department of Energy (Contract No. 89233218CNA000001), with partial support from NASA grant 80HQTR19T0058 and contract NASS-017072. The RAM-SCB model is available at https://github.com/lanl/RAM-SCB. The simulation data is available in https://zenodo.org/record/3943708. Simulations were performed on TianHe-2 at National Supercomputer Center in Guangzhou, China. The authors thank Dr.Xiaojia Zhang for the useful discussions.

References

Chen, M. W., C. L. Lemon, J. Hecht, S. Sazykin, R. A. Wolf, A. Boyd, and P. Valek (2019), Diffuse Auroral Electron and Ion Precipitation Effects on RCM-E Comparisons With Satellite Data During the 17 March 2013 Storm, *Journal of Geophysical Research: Space Physics*, *124*(6), 4194–4216, doi:10.1029/2019JA026545.

Cornwall, J. M., F. V. Coroniti, and R. M. Thorne (1970), Turbulent loss of ring current protons, *Journal of Geophysical Research (1896-1977)*, *75*(25), 4699–4709, doi: 10.1029/JA075i025p04699.

Cowley, S. W. H. (2000), Magnetosphere-Ionosphere Interactions: A Tutorial Review, in *Magnetospheric currents in Geophys. Monograph series*, pp. 91–106.

Fang, X., M. W. Liemohn, J. U. Kozyra, D. S. Evans, A. D. DeJong, and B. A. Emery (2007), Global 30-240 keV proton precipitation in the 17-18 April 2002 geomagnetic storms: 1. Patterns, *Journal of Geophysical Research: Space Physics*, *112*(A5), doi: 10.1029/2006JA011867.

Frey, H. U. (2007), Localized aurora beyond the auroral oval, *Reviews of Geophysics*, *45*(1), doi:10.1029/2005RG000174.

Galand, M., T. Fuller-Rowell, and M. Codrescu (2001), Response of the upper atmosphere to auroral protons, *J. Geophys. Res. Space Physics*, *106*, 127.

Halford, A. J., B. J. Fraser, S. K. Morley, S. R. Elkington, and A. A. Chan (2016),Dependence of EMIC wave parameters during quiet, geomagnetic storm, and geomagnetic storm phase times, *Journal of Geophysical Research: Space Physics*, *121*(7), 6277–6291, doi:10.1002/2016JA022694.

Hardy, D. A., M. S. Gussenhoven, and D. Brautigam (1989), A statistical model of auroral ion precipitation, *Journal of Geophysical Research: Space Physics*, *94*(A1), 370–392, doi: 10.1029/JA094iA01p00370.

Horne, R. B., and R. M. Thorne (1993), On the preferred source location for the convective amplification of ion cyclotron waves, *Journal of Geophysical Research: Space Physics*, *98*(A6), 9233–9247, doi:10.1029/92JA02972.

Horne, R. B., and R. M. Thorne (1994), Convective instabilities of electromagnetic ion cyclotron waves in the outer magnetosphere, *Journal of Geophysical Research: Space Physics*, *99*(A9), 17,259–17,273, doi:10.1029/94JA01259.

Hultqvist, B., W. Riedler, and H. Borg (1976), Ring current protons in the upper atmosphere within the plasmasphere, *Planetary and Space Science*, *24*(8), 783–797, doi:10.1016/0032-0633(76)90115-X.

Jordanova, V. K. (2011), *Self-Consistent Simulations of Plasma Waves and their Effects on Energetic Particles*, in The Dynamic Magnetosphere, IAGA Special Sopron Book Ser., vol. 3, ed. by W. Liu and M. Fujimoto, p. 189, Springer, Dordrecht, 2011.

Jordanova, V. K., J. U. Kozyra, and A. F. Nagy (1996), Effects of heavy ions on the quasi-linear diffusion coefficients from resonant interactions with electromagnetic ion cyclotron waves, *Journal of Geophysical Research: Space Physics*, *101*(A9), 19,771–19,778, doi: 10.1029/96JA01641.

Jordanova, V. K., J. U. Kozyra, A. F. Nagy, and G. V. Khazanov (1997), Kinetic model of the ring current-atmosphere interactions, *Journal of Geophysical Research: Space Physics*, *102*(A7), 14,279–14,291, doi:10.1029/96JA03699.

Jordanova, V. K., C. J. Farrugia, J. M. Quinn, R. M. Thorne, K. E. Ogilvie, R. P. Lepping, G. Lu, A. J. Lazarus, M. F. Thomsen, and R. D. Belian (1998), Effect of wave-particle interactions on ring current evolution for January 10-11, 1997: Initial results, *Geophysical Research Letters*, *25*(15), 2971–2974, doi:10.1029/98GL00649.

Jordanova, V. K., C. J. Farrugia, R. M. Thorne, G. V. Khazanov, G. D. Reeves, and M. F. Thomsen (2001), Modeling ring current proton precipitation by electromagnetic ion cyclotron waves during the May 14-16, 1997, storm, *Journal of Geophysical Research: Space Physics*, *106*(A1), 7–22, doi:10.1029/2000JA002008.

Jordanova, V. K., Y. S. Miyoshi, S. Zaharia, M. F. Thomsen, G. D. Reeves, D. S. Evans, C. G. Mouikis, and J. F. Fennell (2006), Kinetic simulations of ring current evolution during the Geospace Environment Modeling challenge events, *Journal of Geophysical Research: Space Physics*, *111*(A11), doi:10.1029/2006JA011644, a11S10.

Jordanova, V. K., M. Spasojevic, and M. F. Thomsen (2007), Modeling the electromagnetic ion cyclotron wave-induced formation of detached subauroral proton arcs, *Journal of Geophysical Research: Space Physics*, *112*(A8), doi:10.1029/2006JA012215.

Jordanova, V. K., S. Zaharia, and D. T. Welling (2010), Comparative study of ring current development using empirical, dipolar, and self-consistent magnetic field simulations, *Journal of Geophysical Research: Space Physics*, *115*(A12), doi:10.1029/2010JA015671, a00J11.

Jordanova, V. K., D. T. Welling, S. G. Zaharia, L. Chen, and R. M. Thorne (2012), Modeling ring current ion and electron dynamics and plasma instabilities during a high-speed stream driven storm, *Journal of Geophysical Research: Space Physics*, *117*(A9), doi: 10.1029/2011JA017433, a00L08.

Keika, K., K. Takahashi, A. Y. Ukhorskiy, and Y. Miyoshi (2013), Global characteristics of electromagnetic ion cyclotron waves: Occurrence rate and its storm dependence, *Journal of Geophysical Research: Space Physics*, *118*(7), 4135–4150, doi:10.1002/jgra.50385.

Kersten, T., R. B. Horne, S. A. Glauert, N. P. Meredith, B. J. Fraser, and R. S. Grew (2014), Electron losses from the radiation belts caused by EMIC waves, *Journal of Geophysical Research: Space Physics*, *119*(11), 8820–8837, doi:10.1002/2014JA020366.

Khazanov, G. V., K. V. Gamayunov, D. L. Gallagher, J. U. Kozyra, and M. W. Liemohn (2007), Self-consistent model of magnetospheric ring current and propagating electromagnetic ion cyclotron waves: 2. Wave-induced ring current precipitation and thermal electron heating, *Journal of Geophysical Research: Space Physics*, *112*(A4), doi:10.1029/2006JA012033.

Korth, A., G. Kremser, S. Perraut, and A. Roux (1984), Interaction of particles with ion cyclotron waves and magnetosonic waves. Observations from GEOS 1 and GEOS 2, *Planetary and Space Science*, *32*(11), 1393 – 1406, doi:10.1016/0032-0633(84)90082-5.

Loto'aniu, T. M., B. J. Fraser, and C. L. Waters (2005), Propagation of electromagnetic ion cyclotron wave energy in the magnetosphere, *Journal of Geophysical Research: Space Physics*, *110*(A7), doi:10.1029/2004JA010816.

Lui, A. T. Y., D. Venkatesan, C. D. Anger, S. I. Akasofu, W. J. Heikkila, J. D. Winningham, and J. R. Burrows (1977), Simultaneous observations of particle precipitations and auroral emissions by the Isis 2 satellite in the 19-24 MLT sector, *Journal of Geophysical Research (1896-1977)*, *82*(16), 2210–2226, doi:10.1029/JA082i016p02210.

Lyons, L. R. (1992), Formation of auroral arcs via magnetosphere-ionosphere coupling, *Rev. of Geophys.*, *30*, 93–112.

Meredith, N. P., R. B. Horne, T. Kersten, B. J. Fraser, and R. S. Grew (2014), Global morphology and spectral properties of EMIC waves derived from CRRES observations, *Journal of Geophysical Research: Space Physics*, *119*(7), 5328–5342, doi:10.1002/2014JA020064.

Merkin, V. G., A. S. Sharma, K. Papadopoulos, G. Milikh, J. Lyon, and C. Goodrich (2005), Global MHD simulations of the strongly driven magnetosphere: Modeling of the transpolar potential saturation, *Journal of Geophysical Research: Space Physics*, *110*(A9), doi:10.1029/2004JA010993.

Morley, S. K., S. T. Ables, M. D. Sciffer, and B. J. Fraser (2009), Multipoint observations of Pc1-2 waves in the afternoon sector, *Journal of Geophysical Research: Space Physics*, *114*(A9), doi:10.1029/2009JA014162.

Newell, P. T., K. Liou, and G. R. Wilson (2009), Polar cap particle precipitation and aurora: Review and commentary, *J. Atmos. Terr. Phys.*, *71*, 199–215.

Ni, B., X. Thorne, Richard M. Zhang, J. Bortnik, Z. Pu, L. Xie, Z.-j. Hu, D. Han, R. Shi, C. Zhou, and X. Gu (2016), Origins of the earths diffuse auroral precipitation, *Space Science Reviews*, *200*(1), 205–259, doi:10.1007/s11214-016-0234-7.

Park, J., H. Lühr, and J. Rauberg (2013), Global characteristics of Pc1 magnetic pulsations during solar cycle 23 deduced from CHAMP data, *Annales Geophysicae*, *31*(9), 1507–1520, doi:10.5194/angeo-31-1507-2013.

Park, J.-S., K.-H. Kim, K. Shiokawa, D.-H. Lee, E. Lee, H.-J. Kwon, H. Jin, and G. Jee (2016), EMIC waves observed at geosynchronous orbit under quiet geomagnetic conditions (Kp $\leq$ 1), *Journal of Geophysical Research: Space Physics*, *121*(2), 1377–1390, doi:10.1002/2015JA021968.

Popova, Y. A. G. D. A. G., T. A., and S. A. Chernyaeva (2018), Generation of EMIC Waves in the Magnetosphere and Precipitation of Energetic Protons: Comparison of the Data from THEMIS High Earth Orbiting Satellites and POES Low Earth Orbiting Satellites, *Geomagnetism and Aeronomy*, *58*(4), 469–482, doi:10.1134/S0016793218040114.

Prölss, G. W. (1995), Ionospheric F-region storms, *In :H., Volland (Ed.), Handbook of Atmospheric Electrodynamics*, *2*, 195–248.

Ridley, A. J., T. I. Gombosi, and D. L. DeZeeuw (2004), Ionospheric control of the magnetosphere: conductance, *Ann. Geophys.*, *22*, 567–584.

Saikin, A. A., J.-C. Zhang, R. C. Allen, C. W. Smith, L. M. Kistler, H. E. Spence, R. B. Torbert, C. A. Kletzing, and V. K. Jordanova (2015), The occurrence and wave properties of H+-, He+-, and O+-band EMIC waves observed by the Van Allen Probes, *Journal of Geophysical Research: Space Physics*, *120*(9), 7477–7492, doi:10.1002/2015JA021358.

Saikin, A. A., J.-C. Zhang, C. W. Smith, H. E. Spence, R. B. Torbert, and C. A. Kletzing (2016), The dependence on geomagnetic conditions and solar wind dynamic pressure of the spatial distributions of EMIC waves observed by the Van Allen Probes, *Journal of Geophysical Research: Space Physics*, *121*(5), 4362–4377, doi:10.1002/2016JA022523.

Saikin, A., V. Jordanova, J. Zhang, C. Smith, H. Spence, B. Larsen, G. Reeves, R. Torbert, C. Kletzing, I. Zhelavskaya, and Y. Shprits (2018), Comparing simulated and observed EMIC wave amplitudes using in situ Van Allen Probes' measurements, *Journal of Atmospheric and Solar-Terrestrial Physics*, *177*, 190–201, doi: https://doi.org/10.1016/j.jastp.2018.01.024.

Saikin, A. A. (2018), The Spatial Distributions, Wave Properties, and Generation Mechanisms of Inner Magnetosphere EMIC waves, Doctoral Dissertations *2428*, https://scholars.unh.edu/dissertation/2428.

Sakaguchi, K., K. Shiokawa, Y. Miyoshi, Y. Otsuka, T. Ogawa, K. Asamura, and M. Connors (2008), Simultaneous appearance of isolated auroral arcs and Pc 1 geomagnetic pulsations at subauroral latitudes, *Journal of Geophysical Research: Space Physics*, *113*(A5), doi: 10.1029/2007JA012888.

Semenova, N. V., A. G. Yahnin, T. A. Yahnina, and A. G. Demekhov (2019), Properties of localized precipitation of energetic protons equatorward of the isotropic boundary, *Geophysical Research Letters*, *46*(20), 10,932–10,940, doi:10.1029/2019GL085373.

Sergeev, B. G. R., V. A., and P. T. Newell (1997), Dayside isotropic precipitation of energetic protons, *Annales Geophysicae*, *15*(10), 1233–1245, doi:10.1007/s00585-997-1233-5.

Sergeev, V., E. Sazhina, N. Tsyganenko, J. Lundblad, and F. Soraas (1983), Pitch-angle scattering of energetic protons in the magnetotail current sheet as the dominant source of their isotropic precipitation into the nightside ionosphere, *Planetary and Space Science*, *31*(10), 1147–1155, doi:10.1016/0032-0633(83)90103-4.

Shreedevi, P. R., S. V. Thampi, D. Chakrabarty, R. K. Choudhary, T. K. Pant, A. Bhardwaj, and S. Mukherjee (2016), On the latitudinal changes in ionospheric electrodynamics and composition based on observations over the 76-77°E meridian from both hemispheres during a geomagnetic storm, *J. Geophys. Res. Space Physics*, *121*, doi:10.1002/2015JA021841.

Soraas, F., J. Lundblad, N. Maltseva, V. Troitskaya, and V. Selivanov (1980), A comparison between simultaneous I.P.D.P. groundbased observations and observations of energetic protons obtained by satellites, *Planetary and Space Science*, *28*(4), 387–405, doi: 10.1016/0032-0633(80)90043-4.

Soraas, F., K. Aarsnes, J. Lundblad, and D. Evans (1999), Enhanced pitch angle scattering of protons at mid-latitudes during geomagnetic storms, *Physics and Chemistry of the Earth, Part C: Solar, Terrestrial and Planetary Science*, *24*(1), 287 – 292, doi: https://doi.org/10.1016/S1464-1917(98)00041-5.

Tian, X., Y. Yu, and C. Yue (2020), Statistical survey of storm-time energetic particle precipitation, *Journal of Atmospheric and Solar-Terrestrial Physics*, *199*(1364-6826), 105,204, doi:10.1016/j.jastp.2020.105204.

Usanova, M. E., I. R. Mann, J. Bortnik, L. Shao, and V. Angelopoulos (2012), THEMIS observations of electromagnetic ion cyclotron wave occurrence: Dependence on AE, SYMH, and solar wind dynamic pressure, *Journal of Geophysical Research: Space Physics*, *117*(A10), doi:10.1029/2012JA018049.

Vasyliunas, V. M. (1970), Mathematical models of magnetospheric convection and its coupling to the ionosphere, in *Particules and Fields in the Magnetosphere*, edited by B. M. M. Cormac, pp. 60–71, Springer Netherlands.

Vorobjev, Y. O. I., V. G., and E. E. Antonova (2015), Features of the planetary distribution of ion precipitation at different levels of magnetic activity, *Geomagnetism and Aeronomy*, *55*(5), 585–595, doi:10.1134/S0016793215050187.

Walt, M., and H. D. Voss (2004), Proton precipitation during magnetic storms in August through November 1998, *Journal of Geophysical Research: Space Physics*, *109*(A2), doi:10.1029/2003JA010083.

Yahnin, Y. T. A. S. N. V. P. T. A., A. G., and A. G. Demekhov (2018), Proton Auroras Equatorward of the Oval as a Manifestation of the Ion-Cyclotron Instability in the Earth's Magnetosphere (Brief Review), *Geomagnetism and Aeronomy*, *58*(5), 577–585, doi:10.1134/S001679321805016X.

Yahnina, T. A., and A. G. Yahnin (2014), Proton precipitation to the equator of the isotropic boundary during the geomagnetic storm on November 20-29, 2003, 2003, *Cosmic Research*, *52*(1), 79–85, doi:10.1134/S0010952514010092.

Yahnina, T. A., A. G. Yahnin, J. Kangas, J. Manninen, D. S. Evans, A. G. Demekhov, V. Y. Trakhtengerts, M. F. Thomsen, G. D. Reeves, and B. B. Gvozdevsky (2003), Energetic particle counterparts for geomagnetic pulsations of Pc1 and IPDP types, *Annales Geophysicae*, *21*(12), 2281–2292, doi:10.5194/angeo-21-2281-2003.

Young, D. T., H. Balsiger, and J. Geiss (1982), Correlations of magnetospheric ion composition with geomagnetic and solar activity, *Journal of Geophysical Research: Space Physics*, *87*(A11), 9077–9096, doi:10.1029/JA087iA11p09077.

Yu, X., Z. Yuan, S. Huang, D. Wang, H. Li, Z. Qiao, and F. Yao (2017), EMIC waves covering wide L shells: MMS and Van Allen Probes observations, *Journal of Geophysical Research: Space Physics*, *122*(7), 7387–7395, doi:10.1002/2017JA023982.

Yu, Y., V. K. Jordanova, A. J. Ridley, J. M. Albert, R. B. Horne, and C. A. Jeffery (2016), A new ionospheric electron precipitation module coupled with RAM-SCB within the geospace general circulation model, *Journal of Geophysical Research: Space Physics*, *121*(9), 8554–8575, doi:10.1002/2016JA022585.

Yu, Y., V. K. Jordanova, R. M. McGranaghan, and S. C. Solomon (2018), Self-consistent modeling of electron precipitation and responses in the ionosphere: Application to low-altitude energization during substorms, *Geophysical Research Letters*, *45*(13), 6371–6381, doi:10.1029/2018GL078828.

Yu, Y., X. Tian, and V. K. Jordanova (2020), The effects of field line curvature (FLC) scattering on ring current dynamics and ionospheric electrodynamics, *Earth and Space Science Open Archive*, p. 30, doi:10.1002/essoar.10502120.1.

Zaharia, S., V. K. Jordanova, M. F. Thomsen, and G. D. Reeves (2006), Self-consistent modeling of magnetic fields and plasmas in the inner magnetosphere: Application to a geomagnetic storm, *Journal of Geophysical Research: Space Physics*, *111*(A11), doi:10.1029/2006JA011619, a11S14.

Zhang, X.-J., W. Li, R. M. Thorne, V. Angelopoulos, J. Bortnik, C. A. Kletzing, W. S. Kurth, and G. B. Hospodarsky (2016), Statistical distribution of EMIC wave spectra: Observations from Van Allen Probes, *Geophysical Research Letters*, *43*(24), 12,348–12,355, doi:10.1002/2016GL071158.

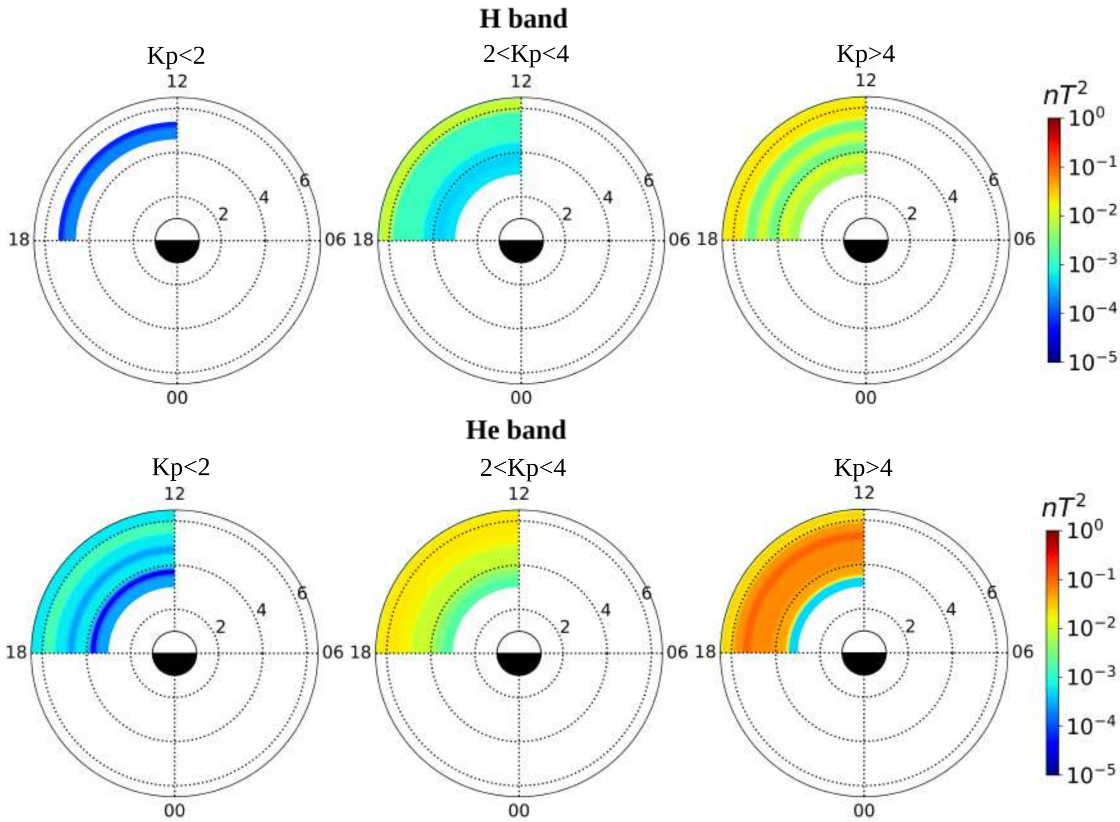

761 **Figure 1.** EMIC Wave model 1: Intensities of H-band (top panel) and He-band (bottom panel)
762 EMIC waves from the Combined Release and Radiation Effects (CRRES) satellite measurements.

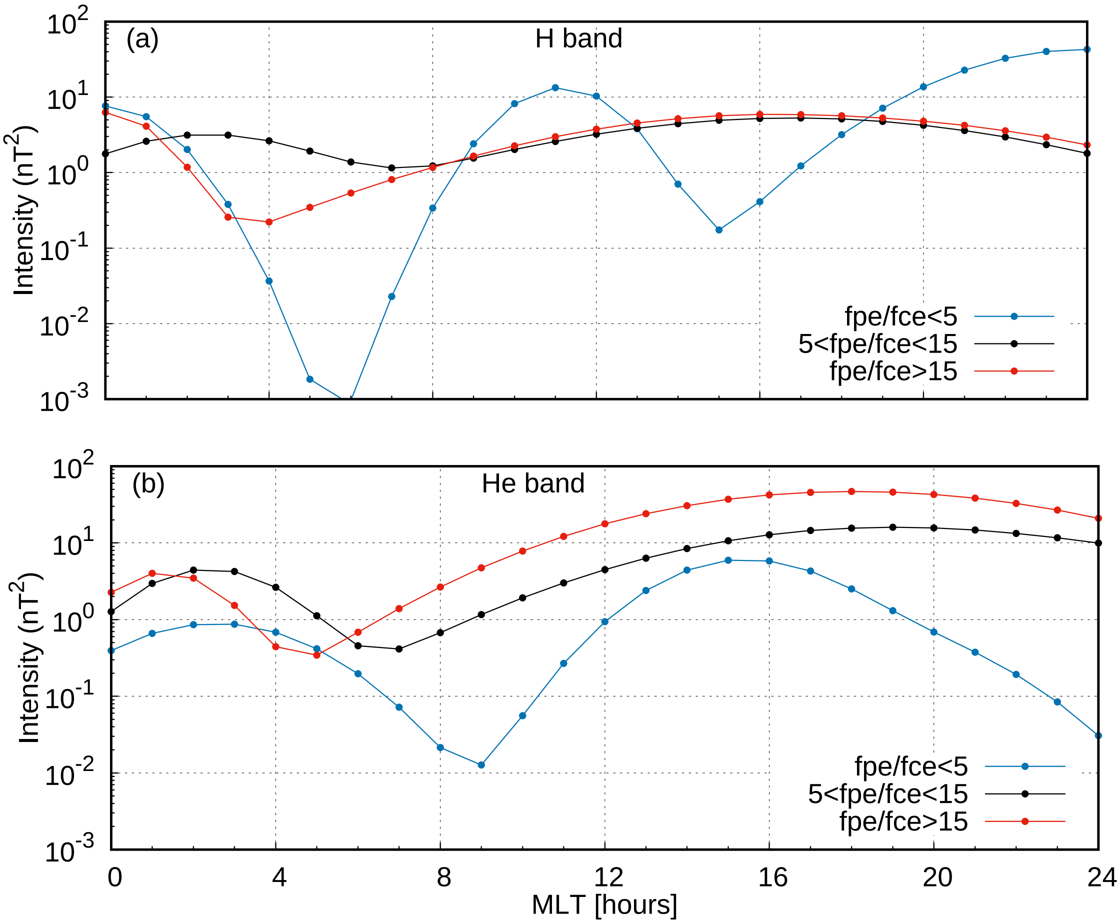

Figure 2. EMIC wave model 2: Intensities of H-band (panel (a)) and He-band (panel (b)) EMIC waves obtained from the EMIC wave frequency spectra constructed using the Van Allen Probes measurements. The EMIC wave intensities are parameterized by the f_{pe}/f_{ce}

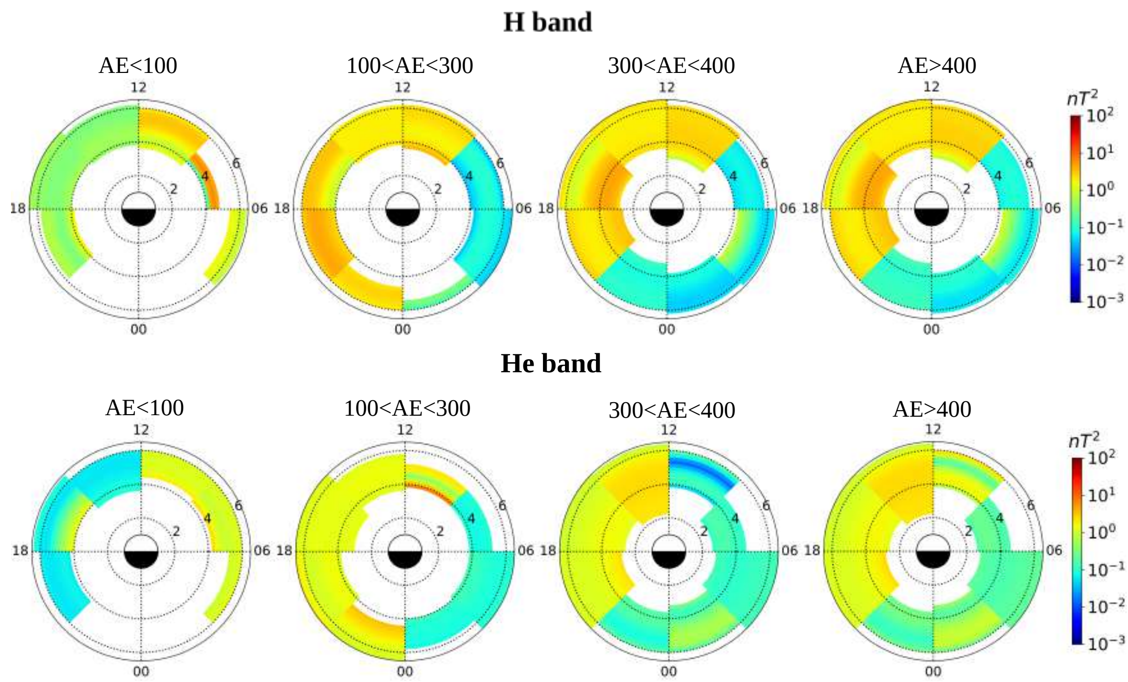

Figure 3. EMIC wave model 3: Intensities of H-band (top panel) and He-band (bottom panel) EMIC waves based on the Van Allen Probes measurements for varying levels of geomagnetic activity indicated by the AE index.

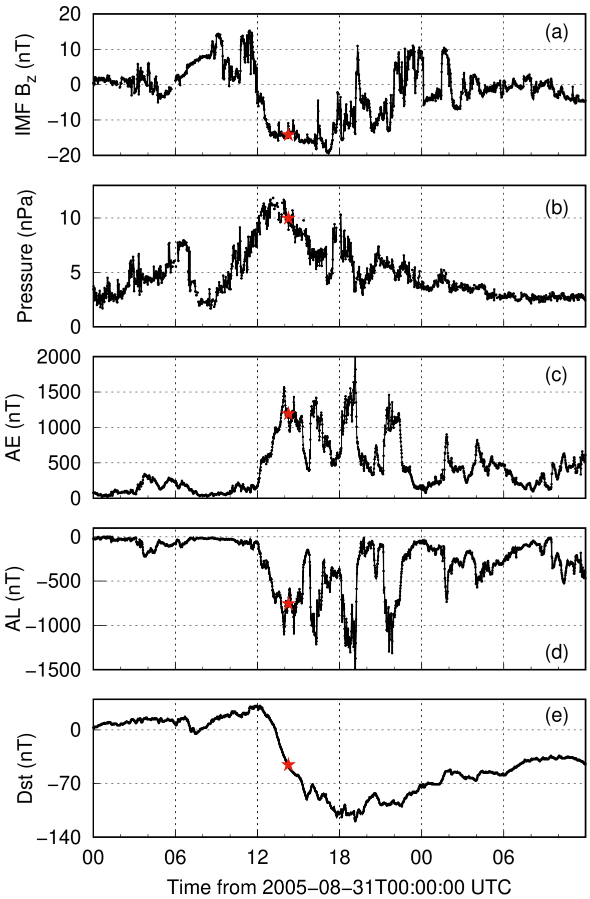

Figure 4. Solar wind and geomagnetic conditions during 31 August 2005: In panels (a) - (e) are shown the IMF B_z, solar wind pressure, AE index, AL index and Sym H respectively. The black vertical line marks the beginning of the main phase of the storm. The red stars mark the selected times at which the simulation results are presented in Figures.

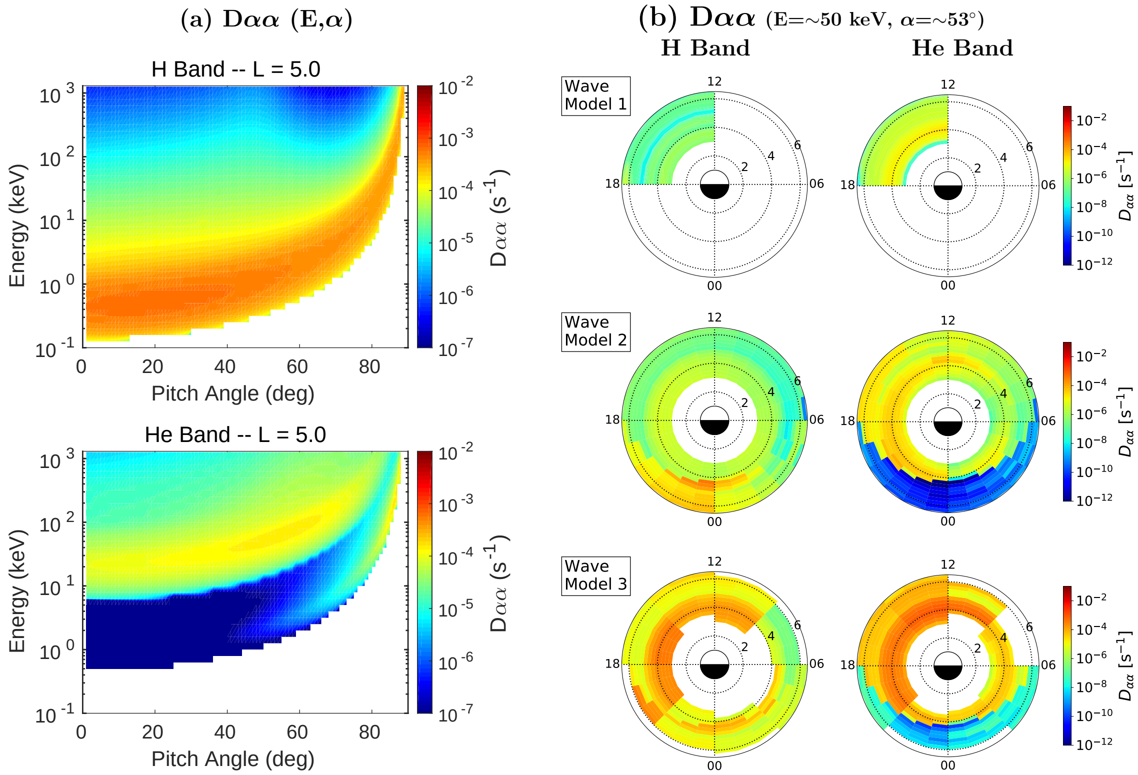

773 **Figure 5.** Panel (a) : Bounce averaged pitch angle diffusion coefficients due to H-band and He-band EMIC waves at L=5 with f_{pe}/f_{ce}=14. Panel (b): Global distribution of diffusion coefficients in the equatorial plane due to H and He-band at 1400 UT on 31 August 2005 in the simulations with the EMIC wave model 1, 2 and 3 respectively. The diffusion coefficients in panel (b) are those for protons with E=50 keV and pitch angle 53°

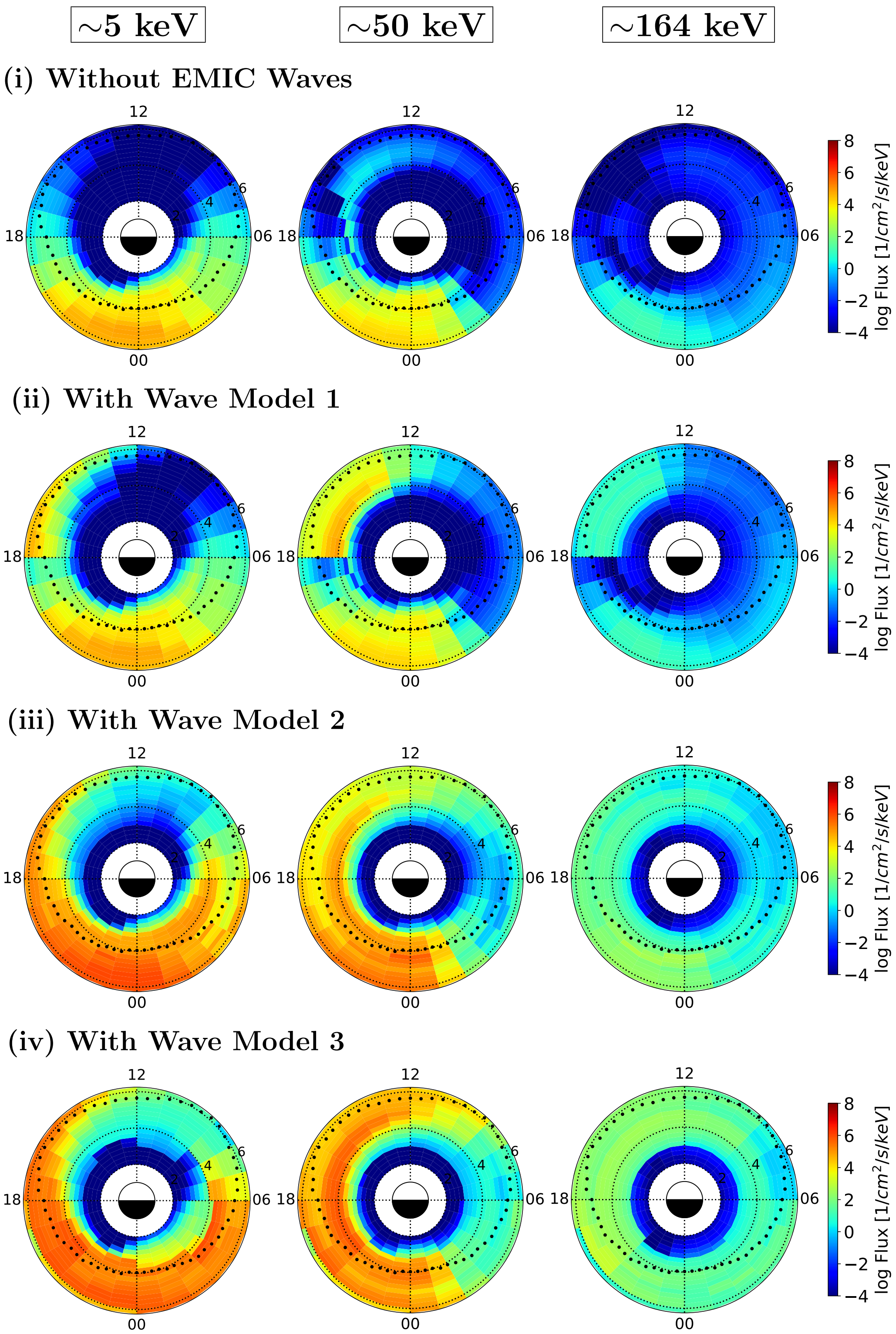

778 **Figure 6.** Panels (i)-(iv) shows the global distribution of proton precipitating fluxes (E=~5 keV, ~50 keV and ~164 keV) obtained from RAM-SCBE simulations (i) without EMIC waves, with (ii)EMIC wave model 1 (iii)EMIC wave model 2 and (iv)EMIC model 3. The plots are shown at 1400 UT (main phase of the storm) on 31 August 2005.

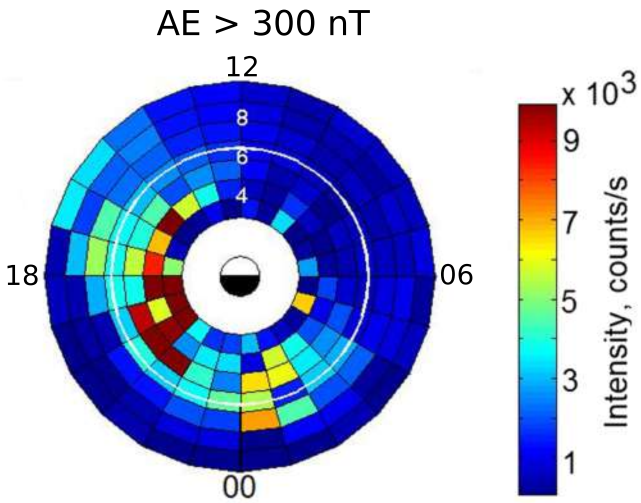

Figure 7. Intensity of localized precipitation of energetic protons (30-80 keV) at AE>300 nT [*Semenova et al.*, 2019].

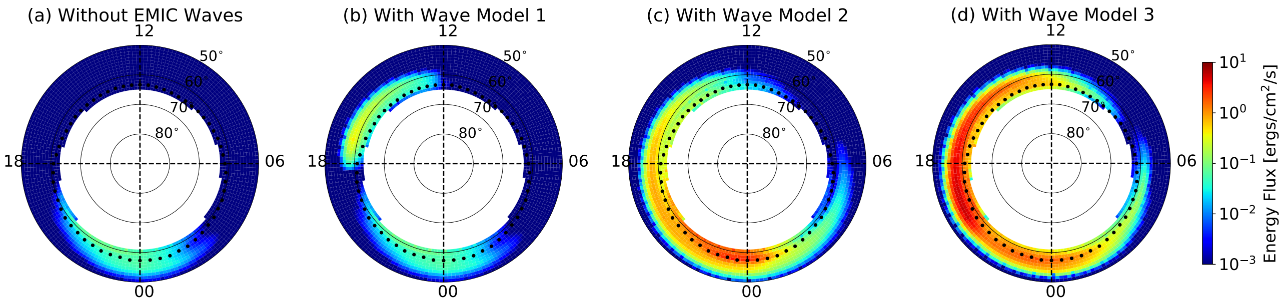

Figure 8. Precipitating energy flux at 1400 UT (main phase) obtained from the RAM-SCBE simulations (a) without EMIC waves and (b)-(d) with EMIC wave model 1, 2 and 3 respectively

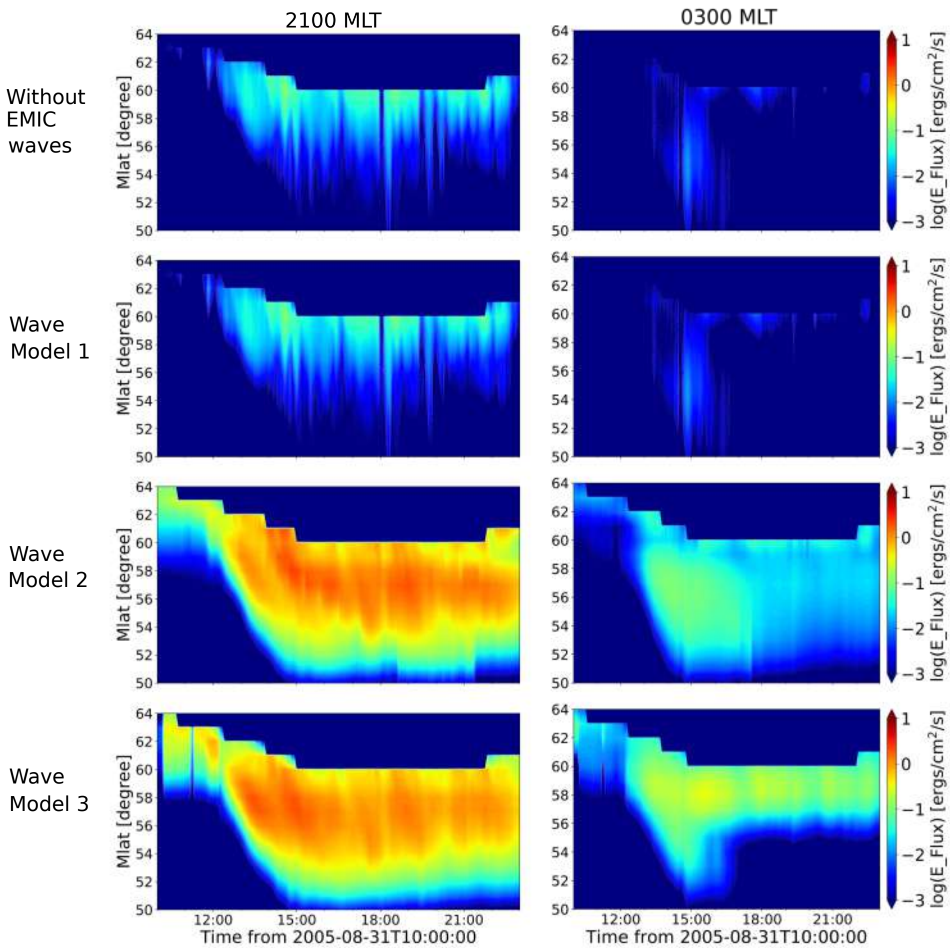

Figure 9. Distribution of precipitating energy flux obtained from the RAM-SCBE simulations without EMIC waves and using EMIC wave model 1, 2 and 3. The left panel shows the precipitating energy flux at 2100 MLT while the right panel shows the precipitating energy flux at 0300 MLT.

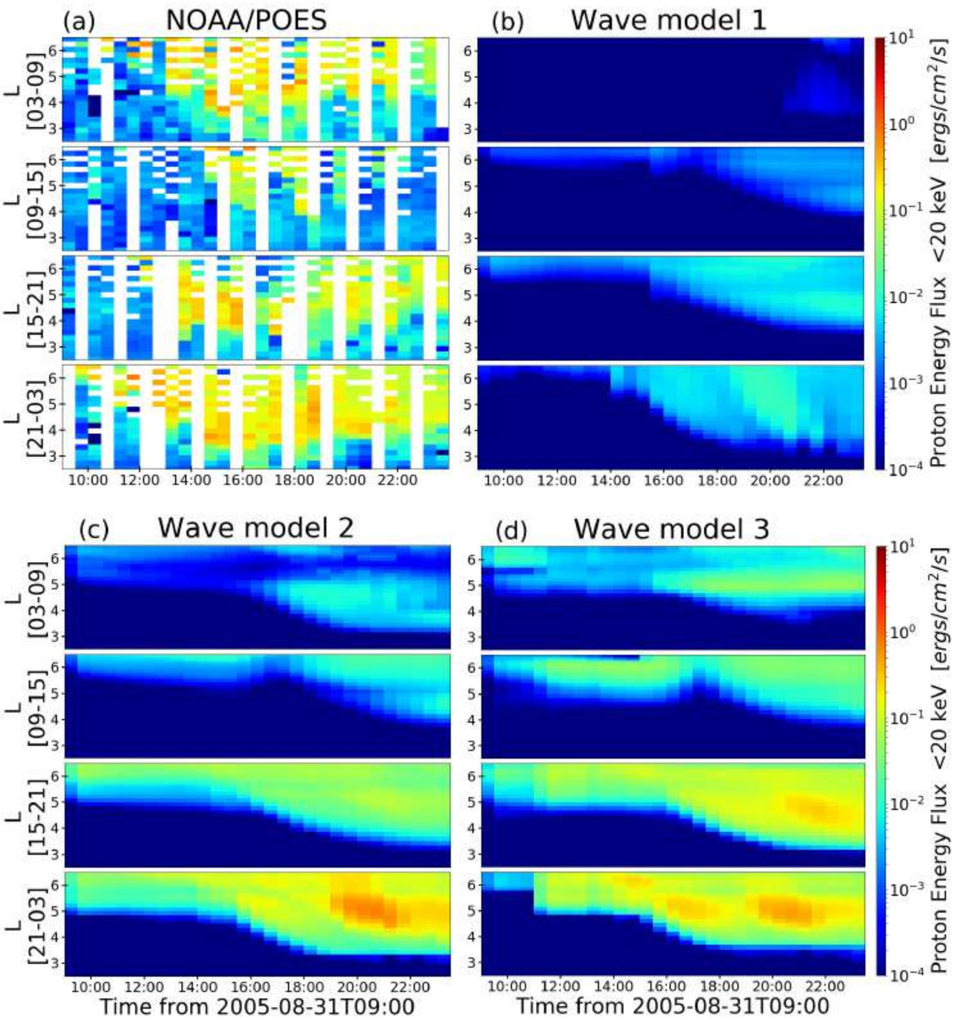

Figure 10. Comparison of NOAA/POES satellite measurements with the RAM-SCBE simulations with and without EMIC waves for 31 August 2005: Panels (a)-(d) shows the proton energy flux of E<20keV at different MLT sectors.

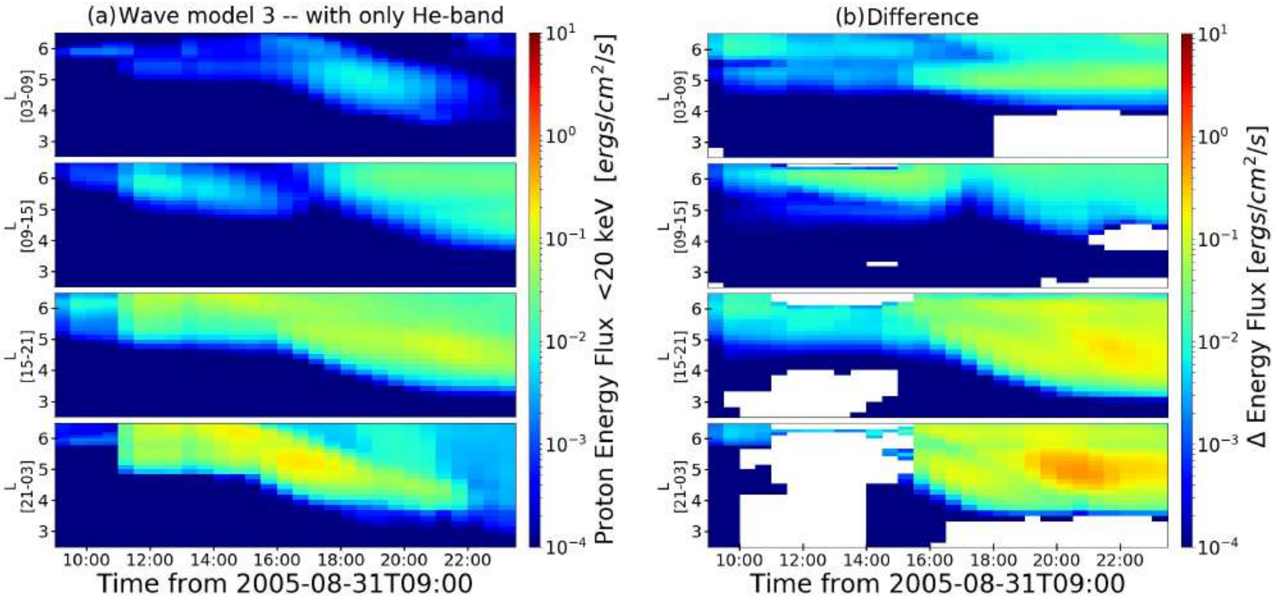

792 **Figure 11.** Panel (a) shows the RAM-SCBE simulations with only He-band EMIC waves in the wave model 3. Panel (b) shows the difference in the proton energy flux (E<20keV) between the simulations with both H-band and He-band EMIC waves in the wave model 3 and only He-band EMIC waves in the wave model 3.

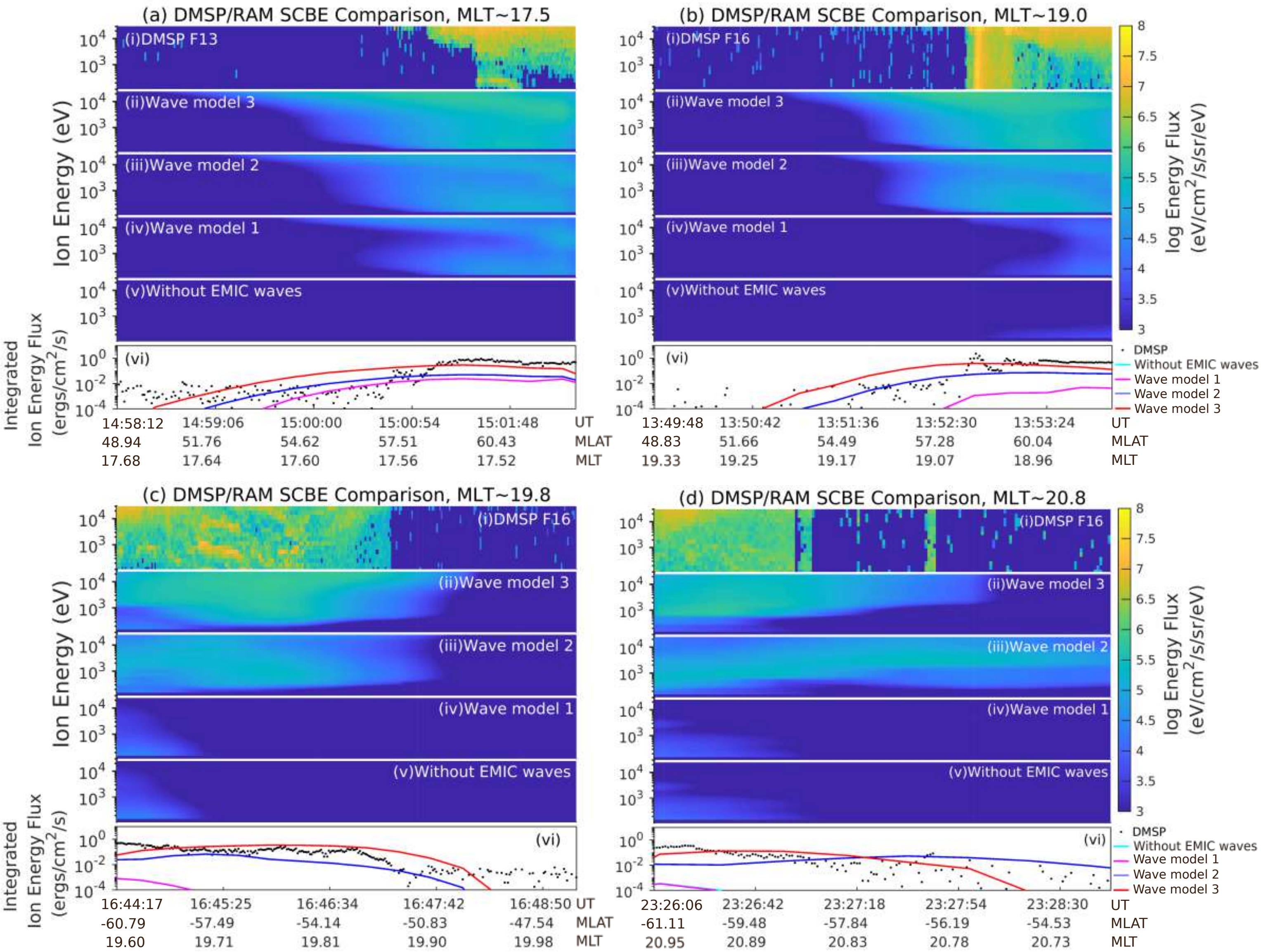

Figure 12. Comparison of DMSP F16 satellite measurements with the RAM-SCBE simulations with and without EMIC waves for 31 August 2005: Panel (i) shows the DMSP F16 energy spectrogram of ions in log scale. Panels (ii)-(v) shows the energy spectrogram of ions from simulations. Panel (vi) shows the integrated ion energy flux.